crystals

MDPI

Article

Crystal Structure Dependence of the Energy Transfer from Tb(III) to Yb(III) in Metal–Organic Frameworks Based in Bispyrazolylpyridines

Paloma Martinez-Martin [1], Josefina Perles [2] and Juan Carlos Rodriguez-Ubis [1,*]

[1] Departmento de Química Orgánica, Facultad de Ciencias Universidad Autónoma de Madrid, 28049 Madrid, Spain; paloma.martinezm@uam.es

[2] Single Crystal X-ray Diffraction Laboratory, Servicio Interdepartamental de Investigación, Universidad Autónoma de Madrid, 28049 Madrid, Spain; josefina.perles@uam.es

* Correspondence: jcrubis@uam.es

Received: 21 December 2019; Accepted: 22 January 2020; Published: 27 January 2020

Abstract: Luminescent mixed lanthanide metal–organic framwork (MOF) materials have been prepared from two polyheterocyclic diacid ligands, 2,6-bis(3-carboxy-1-pyrazolyl)pyridine and 2,6-bis(4-carboxy-1-pyrazolyl)pyridine. The crystal structures of the two organic molecules are presented together with the structures for the MOFs obtained by hydrothermal synthesis either with Yb(III) or mixed Tb(III)/Yb(III) ions. Different coordination architectures result from each ligand, revealing also important differences between the lanthanides. The mixed lanthanide metal–organic frameworks also present diverse luminescent behavior; in the case of 2,6-bis(4-carboxy-1-pyrazolyl)pyridine, where no coordinated water is present in the metal environment, Tb(III) and Yb(III) characteristic emission is observed by excitation of the bispyrazolylpyridine chromophore.

Keywords: lanthanide luminescence; energy transfer; Tb(III)/Yb(III) ions; LnMOF; topology; coordination polymers

1. Introduction

In the last few decades new hybrid coordination materials or MOFs (metal–organic frameworks) have been emerging as very promising materials for applications in different fields. Generally, a hybrid material is obtained from metal cations and organic ligands that act as linkers between them establishing coordination bonds. In these materials, further self-assembly is often achieved through less energetic interactions such as hydrogen bonds, $\pi\pi$-stacking and van der Waals or electrostatic forces. These MOFs may have luminescent properties, depending on the organic linkers and metal centers employed. Advances in the outstanding luminescent properties of the lanthanide ions have situated MOFs based on these ions (LnMOFs) in the focus of interesting developments for these materials such as optics, electronics, and biomedicine [1–3]. Lanthanide luminescence performance is based on the interesting properties of these ions, as high quantum yields, long lifetimes, narrow emission bands or energy transfer processes. Furthermore, their emission range can cover from the UV to the NIR area (300–1550 nm), pushing them to the vanguard of luminescence-based hybrid materials, since they combine typical MOFs' properties, such as porosity, with excellent opportunities to shape new photophysical properties for the development of advanced materials [4].

In this context, many of the exciting properties of these ions as sharp emission lines, long excited-state lifetimes, large Stokes and anti-Stokes emissions, as well as high quantum yields, take a special relevance in heterolanthanide MOFs where coordination modes or relative distance

among ions are extremely dependent on the coordination environment of the metals. The chemical nature of the linker and the geometry of the potential coordinating groups both play a crucial role in the resulting crystalline lattice and therefore, in the properties of the materials [5,6].

Concerning the lanthanide ions, these metals present a weak light absorption, because f–f transitions are forbidden by Laporte's rule and they have low molar absorption coefficients. As a consequence, they need high energy intensity to be directly excited. These limitations can be solved by using an organic ligand that triggers a higher emission of the lanthanide, acting as an antenna to collect the incident radiation and transfer it to the metal ion [7].

In mixed-metal LnMOFs, energy transfer might also occur from lanthanide ions with energetically higher levels to others where these states are at lower energies [8]. This enhancement and/or quenching of the photoluminescence emission has been reported by terbium sensitization of the less emissive europium ion in heterolanthanide coordination polymers [9,10]. In addition to Eu(III) and Tb(III) ions, those lanthanides that emit in the NIR spectrum section such as Yb(III), Nd(III) and Er(III) are more sensitive to deactivation by nonradiative processes as couplings with high-energy oscillators present in the solvent molecules or on the ligands. In order to enhance NIR light-emitting lanthanide luminescence, most of the examples described in the literature are based on Ln-orthophosphates [11,12], co-doped glass ceramics [13], or silica sol–gel glasses [14,15], where properties may be tuned by adjusting parameters as the concentration and/or the type of lanthanide, as well as the nature and size of the host crystals. An adequate design of the MOF architecture, targeting the geometry and the photophysical properties of the organic linker, should be advantageous in order to optimize the synthetic procedures and to control the crystal structures of new mixed-metal LnMOFs.

Regarding the organic molecules acting as linkers, tris-N-heterocyclic ligands continue to be very widely used in complexation chemistry, because of their synthetic flexibility, strong metal binding capacity, and their ability to impart distinct photophysical, electrochemical, and magnetic properties. Terpyridine and its derivatives are still among the most commonly used poly-heterocyclic linkers, as they have shown excellent properties in different fields as supramolecular chemistry, soft macromolecular chemistry, MOFs construction or nanoscience [16]. However, other classes of tris-N-heterocycles such as 2,6-diazolylpyridines have certain advantages over terpyridines, such as their synthetic versatility. In particular, 2,6-dipyrazolyl, 2,6-dibenzimidazolyl, and 2,6-diindazolyl pyridines are among the most studied [17].

We are especially interested in a new family of organic linkers based on the 2,6-bis(pyrazol-1-il)pyridine framework, which provides a cavity for lanthanide chelation optimal to enhance the luminescent emission properties of the ion by antenna effect. This kind of skeleton offers the combination of good bispyrazolyl pyridine chelating properties along with the rigidity of pyrazole rings, being both important requirements for MOF architectures [18]. The core of these polyaromatic ligands (providing a planar environment that could drive to π–π stacking) and the existence of carboxylic groups in different positions on the pyrazole rings are the most relevant structural characteristics controlling the coordination and the building of supramolecular structures. These carboxylic groups will help the extension of supramolecular structures through the space based on metal-ligand coordination, given the known affinity of the lanthanide ions for electron donor atoms such as oxygen.

In this work, we report the crystal structures of 2,6-bis(3-carboxy-1-pyrazolyl)pyridine (H_2L^3) and 2,6-bis(4-carboxy-1-pyrazolyl)pyridine (H_2L^4) (Scheme 1), and the solvothermal reaction of these two molecules with either Yb(III) or a mixture of Tb(III) and Yb(III) to prepare their respective MOFs. The crystal structures of the four new LnMOFs (YbL^3, YbL^4, Tb/YbL^3, and Tb/YbL^4) are also described and compared. The different orientation of the carboxylic groups in relation with the trisheterocyclic entity drives to diverse crystal architectures in the resulting MOFs and consequently, to different luminescence behaviors. Finally, this study compares the capabilities of NIR sensitization of Yb(III) by direct excitation of the ligand and by means of a double energy transfer ligand→Tb(III)→Yb(III) in the case of Tb(III)/Yb(III) heterolanthanide MOFs.

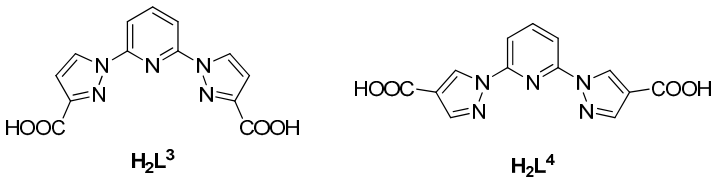

Scheme 1. Organic linkers 2,6-bis(3-carboxy-1-pyrazolyl)pyridine (H_2L^3) and 2,6-bis(4-carboxy-1-pyrazolyl)pyridine (H_2L^4).

2. Materials and Methods

2.1. Physical Measurements

All reagents used were of reagent grade and the solvents were distilled prior to their use. Lanthanide nitrate salts were purchased from Aldrich and used as received. Infrared spectra were recorded by ATR Infrared (IR) spectroscopy with a Spectrum Two Perkin Elmer spectrometer (PerkinElmer, Inc.; Waltham, NY, USA), equipped with a diamond crystal, in the 4000–450 cm^{-1} range. Elemental analysis measurements were conducted with a LECO CHNS-932 (Model NO: 601-800-500) microelemental analyzer (LECO, St. Joseph, IL, USA). TXRF (Total reflection X-Ray Fluorescence) analysis of the samples was performed with a benchtop S2 PicoFox TXRF spectrometer (Bruker Nano, Berlin, Germany), equipped with a molybdenum X-ray source working at 50 kV, 600 μA and 500 s and a XFlash SDD detector (effective area of 30 mm^2) and an energy resolution better than 150 eV for Mn K_α. The Spectra 7 software package, also from Bruker, was used for control, acquisition, deconvolution, and integration of all analyzed samples.

Spectroscopic measurements in solid state were performed in quartz tubes. Quantum yield measurements were recorded on a Perkin Elmer Lambda 950 spectrometer by integration sphere. Steady-state emission spectra were recorded on a FLS920P fluorescence spectrometer (Edinburgh Instrument) equipped with a 450-W continuous wavelength Xe lamp (range from 230 to 900 nm), using Hamamatsu R928 (visible) or R5509-72 (Vis and NIR range) photomultipliers and phosphorescence lifetimes were measured on the same instrument working in the multi-channel spectroscopy (MCS) mode, using a Xe flash lamp as the excitation source. For steady-state emission in the NIR range, high-pass filters at 850 nm were used to remove second-order artefacts.

Powder X-ray diffractograms (PXRD) were recorded in a Bruker D8 diffractometer with a Sol-X energy dispersive detector, working at 40 kV and 30 mA and employing Cu K_α (λ = 1.5418 Å) filtered radiation. The diffractograms were registered with a step size of 0.02° and exposure time of 0.6 s per step and a 2θ range of 3°–30°.

Single-crystal X-ray diffraction (SCXRD) measurements were collected in a Bruker Kappa Apex II diffractometer using graphite-monochromated Mo K_α radiation (λ = 0.71073 Å). A summary of some crystal and refinement data can be found in Tables 1–3; and more information is collected in the Supplementary Materials (Tables S1, S2, S4, S5, S7, S8, S11, S12, S15, S16, S19, and S20). CCDC 1972548-1972553 contain the crystallographic data for H_2L^3, H_2L^4, YbL^3, YbL^4, Tb/YbL^3, and Tb/YbL^4. These data can be obtained free of charge from the Cambridge Crystallographic Data Centre via www.ccdc.cam.ac.uk/data_request/cif.

Table 1. Crystal and refinement data for H_2L^3 and H_2L^4.

	H_2L^3	**H_2L^4**
Formula	$C_{13}H_9N_5O_4$	$(C_{13}H_9N_5O_4)\cdot(C_2H_3N)_{0.5}$
Space group	*C*2/*c*	*Pnma*
a/Å	10.993(1)	12.171(1)
b/Å	11.891(1)	6.5022(7)
c/Å	9.4100(7)	20.401(2)
α/°	90	90
β/°	93.034(4)	90
ɣ/°	90	90
V/Å^3	1228.3(2)	1614.5(3)
Z	4	4
d calc/*g*·cm^{-3}	1.618	1.309
μ/mm^{-1}	0.125	0.676
R indices ($I > 2\sigma(I)$)	R_1 = 0.0386 wR_2 = 0.0852	R_1 = 0.1017 wR_2 = 0.2867
GooF on F^2	1.014	1.105

Table 2. Crystal and refinement data for YbL^3 and Tb/YbL^3.

	YbL^3	**Tb/YbL^3**
Formula	$[Yb(L^3)(NO_3)(H_2O)_2]_n\cdot 2nH_2O\cdot n(CH_3CN)$	$[Tb_{0.98}Yb_{1.02}(L^3)_3(H_2O)_3]_n$ $2.5n(H_2O)$
Space group	*Pbcn*	$P2_1/n$
a/Å	20.2374(7)	18.0063(9)
b/Å	6.8593(3)	12.3925(7)
c/Å	29.447(1)	24.494(1)
α/°	90	90
β/°	90	106.133(4)
ɣ/°	90	90
V/Å^3	4087.6(3)	5250.5(5)
Z	8	4
d calc/*g*·cm^{-3}	2.009	1.660
μ/mm^{-1}	4.649	3.195
R indices ($I > 2\sigma(I)$)	R_1 = 0.0314 wR_2 = 0.0651	R_1 = 0.0597 wR_2 = 0.1586
GooF on F^2	1.101	1.020

Table 3. Crystal and refinement data for YbL^4 and Tb/YbL^4.

	YbL^4	**Tb/YbL^4**
Formula	$[Yb(L^4)(HL^4)]_n$	$[Tb_{0.38}Yb_{0.62}(HL^4)(NO_3)_2]_n$
Space group	*P*-1	*C*2/*c*
a/Å	4.706(2)	8.634(2)
b/Å	9.193(3)	15.998(2)
c/Å	15.322(6)	12.721(3)
α/°	72.711(9)	90
β/°	88.77(1)	90.69(1)
ɣ/°	86.788(9)	90
V/Å^3	1614.5(3)	1756.9(6)
Z	1	4
d calc/*g*·cm^{-3}	2.020	2.230
μ/mm^{-1}	3.777	4.906
R indices ($I > 2\sigma(I)$)	R_1 = 0.0901 wR_2 = 0.2421	R_1 = 0.0332 wR_2 = 0.0594
GooF on F^2	1.090	1.057

2.2. Synthesis

2.2.1. Synthesis of the Ligands

2,6-Bis(3-carboxy-1-pyrazolyl)pyridine H_2L^3 and 2,6-bis(4-carboxy-1-pyrazolyl)pyridine H_2L^4 were prepared from 2,6-difluoropyridine through aromatic nucleophilic substitution with 3- or 4-ethoxycarbonylpyrazol, followed by saponification of the diester. These procedures had been described previously by our group (in the case of H_2L^3 by a different route). For both H_2L^3 and H_2L^4, the spectral and analytical data are fully in accord with the previously reported [10,19].

2.2.2. Hydrothermal Synthesis of LnMOFs

$Yb(NO_3)_3 \cdot 5H_2O$ (0.3 mmol) was dissolved in distilled water (1 mL). This solution was added to a suspension of the organic ligand (30 mg, 0.1 mmol) in freshly distilled acetonitrile (4 mL). After the mixture was stirred for 30 min, it was placed into a 10 mL Teflon-lined stainless-steel autoclave under autogenous pressure and heated at 120 °C for 120 h. After cooling to room temperature, crystals were collected for SCXRD measurements, and afterwards washed with water and acetone and then dried at room temperature.

YbL^3 Anal. (%) Calcd. for $C_{14}H_{16.5}N_{6.5}O_{11}Yb \cdot 0.75H_2O$: %C = 26.34 %H = 2.84 %N = 14.26 Found: %C = 26.28 %H = 2.79 %N = 14.00. (Bulk weight: 46 mg; Yield: 75%)

YbL^4 Anal. (%) Calcd. for $C_{26}H_{15}N_{10}O_8Yb \cdot 5H_2O$: %C = 36.37 %H = 2.93 %N = 16.31 Found: %C = 35.76 %H = 2.74 %N = 16.36. (Bulk weight: 41 mg; Yield: 53%)

An equimolar mixture of Yb $(NO_3)_3 \cdot 5H_2O$ and Tb $(NO_3)_3 \cdot 5H_2O$, (0.3 mmol) was dissolved in distilled water (1 mL). This solution was added to a suspension of the ligand (30 mg, 0.1 mmol) in freshly distilled acetonitrile (4 mL). After the mixture was stirred for 30 min, it is placed into a 10 mL Teflon-lined stainless-steel autoclave under autogenous pressure and heated at 120 °C for 120 h. After cooling to room temperature, crystals were collected for SCXRD measurements, and afterwards washed with water and acetone and then dried at room temperature.

Tb/YbL^3 Anal. (%) Calcd for $C_{39}H_{21}N_{15}O_{17.50}Tb_{0.98}Yb_{1.02} \cdot 12H_2O$: %C = 30.65 %H = 2.97 %N = 13.75; Found: %C = 30.74 %H = 3.01 %N = 14.03; TXRF: ratio Yb/Tb 51:49. (Bulk weight: 39 mg; Yield: 30%)

Tb/YbL^4Anal. (%) Calcd for $C_{13}H_8N_9O_{10}Tb_{0.38}Yb_{0.62}$: %C = 25.27 %H = 1.30 %N = 20.40; Found: %C = 39.76 %H = 2.27 %N = 17.67; TXRF. ratio Yb/Tb 62/38. (Bulk weight: 37 mg; Yield: 63%)

3. Results and Discussion

Hydrothermal synthesis performed in identical conditions yielded in all cases crystalline materials whose analytical data confirm the structures of the MOFs considering the different molecules of coordinated and interstitial water proved by the single crystal X-ray diffraction structures (see below).

Purity of the samples was confirmed by the comparison of the powder X-ray diffraction measurements performed on the bulk samples with the patterns simulated from SCXRD data (Figures S8, S12, S16, and S20). Some differences in intensity were observed in the experimental patterns due to the preferred orientation of the crystal samples. MOFs obtained from the H_2L^3 ligand were found to be less stable in ambient conditions and consequently, their PRXD patterns reflect some loss of crystallinity (Figures S8 and S16). The theoretical powder patterns simulated from single crystal data of YbL^4 (Figure S12) and Tb/YbL^4 (Figure S20) were corrected with a (013) and (11-2) orientation respectively, applying March−Dollase [20] parameter values of 0.23 and 0.25, to account for the observed needle-like habit.

In the case of the reaction of H_2L^4 with Yb and Tb (Figure S20), a mixture of crystalline materials was obtained, and only the majoritarian phase Tb/YbL^4 could be isolated and characterized in detail. This mixture contains also a phase with the same structural type as the one obtained with Yb (described in Section 3.1 as YbL^4) plus a small amount of another unknown phase (responsible for the peak appearing at $2\Theta = 6.4°$). This impurity also appears in the PRXD pattern of Tb/YbL^3 (Figure S17)

but, seems to have no influence in the luminescent behavior, as proved by the photophysics results (Section 3.2).

The elemental analyses also corroborate the corresponding theoretical values, except in the case of the reaction of H_2L^4 with Yb and Tb, where the values deviate greatly from the theoretical ones for Tb/YbL^4, proving that a mixture of phases is obtained.

Regarding the IR measurements, the absorption bands observed in the range of 3400–3500 cm^{-1} can be attributed to the characteristic peaks of O–H vibrations, both from the water molecules or the protonated carboxylic oxygen atoms in the MOFs derived from H_2L^4. The most remarkable differences between the materials correspond to the vibration bands from the carboxylate groups, as a consequence of the different coordination modes. Thus, in the Figure S15 only the strong vibrations correspond to the symmetric stretching vibration of the bidentate carboxylate group at 1465 and 1330 cm^{-1} appear, while Figure S11 shows the same kind of vibration bands (1427 and 1319 cm^{-1}), together with two new ones at 1564 and 1522cm^{-1} corresponding to the stretching vibration of the monodentate carboxylate groups. This fact is related to the different coordination modes displayed by the carboxylate groups in the compounds. Figure S7 shows the vibration bands (1468 and 1337 cm^{-1}) of bidentate carboxylate and the stretching vibration N-O of the coordinated nitrate anion (1490 cm^{-1}). The IR spectrum of Tb/YbL^4 (Figure S19) shows not only the bands corresponding to the symmetric stretching vibration of the bidentate carboxylate group at 1404 and 1316 cm^{-1}, belonging to structural phase 2, but the stretching vibration N-O of nitrate anion (1483 cm^{-1}) also appears, together with the stretching vibration of the monodentate carboxylate group at 1564 cm^{-1} corresponding to structural phase 1, confirming the coexistence of both phases into the bulk.

3.1. Crystal Structures

H_2L^3 crystallizes in the monoclinic *C*2/*c* space group with half a molecule in the asymmetric unit (Figure S1 in the SI). The H_2L^3 molecule displays an angle between the Pz and the Py rings of 8.10°; and an angle of 12.68° between the two lateral Py rings. Regarding the supramolecular interactions, each molecule is connected with the two neighbor ones by four O-H···O bonds involving both carboxylic groups, to yield chains of molecules (Table S3 and Figure S2). These chains are densely packed parallel to each other, at a distance of 3.461 Å, through π–π interactions.

The structure of H_2L^4 was solved from an acetonitrile cocrystal with formula $(C_{13}H_9N_5O_4)\cdot(C_2H_3N)_{0.5}$. This structure belongs to the orthorhombic *Pnma* space group and the H_2L^4 molecule (Figure S3) lies completely flat, with all of its atoms located in a mirror plane. Each molecule is connected with four neighbor ones by four O-H···N bonds involving both carboxylic groups and N atoms from the pyrazole rings, giving rise to layers parallel to the *ac* plane (Table S6 and Figure S4). There are π–π interactions between these layers, situated at a distance of 3.251 Å. The acetonitrile molecules are located flat in the layers with a 50% random occupation of the available holes.

YbL^3 (Figure 1) is a two-dimensional coordination polymer with formula $[YbL^3(NO_3)(H_2O)_2]_n\cdot 2n(H_2O)\cdot 0.5n(CH_3CN)$. The layers show a thickness of *a*/2 = 10.1187 Å and are parallel to the crystallographic *bc* plane. The asymmetric unit (Figure S5) in this structure contains one metal atom and one fully deprotonated $(L^3)^{2-}$ ligand, as well as a chelating nitrate, two coordinated water molecules and also some disordered interstitial solvent molecules (two water ones and half an acetonitrile). The metal is bonded to eight oxygen atoms in a MO_8 coordination environment (Figure S6 and Table S9), four of them from $(L^3)^{2-}$ ligands (O1, O2, O3, and O4), two of them from a chelating nitrate ligand (O5 and O6) and two from water molecules (O8T and O9T). MO_8 polyhedra are placed in zig-zag chains along the *b* direction, joined by O-C-O bridges, where the metals are separated 5.639 Å, while the metals from different chains are separated by the full length of the organic linkers (15.231 Å). $(L^3)^{2-}$ ligands are coordinated to three different metals in a tridentate μ_3-1κO, 2κO′, 3κ^2O′′, O′′′ fashion. Regarding the planarity of the organic moiety, the torsion of the three rings is highly increased compared to the non-coordinated ligand, with Pz-Py angles of 14.80° and 9.79°, and Pz-Pz of 6.09°. There are weak intralayer hydrogen bonds and π–π interactions,

as well as stronger H-bonds between the layers and the interstitial water and acetonitrile molecules (Table S10).

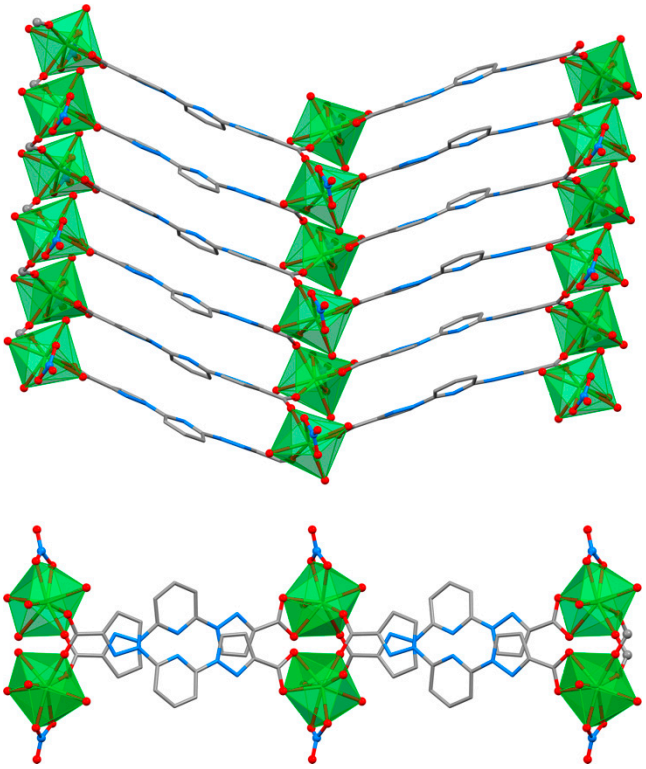

Figure 1. Layer of $[YbL^3(NO_3)(H_2O)_2]_n$ in YbL^3: perpendicular view (**top**) and lateral view (**bottom**).

Compound YbL^4 (Figure 2) is a two-dimensional coordination polymer with formula $[Yb(L^4)(HL^4)]_n$. The layers show a thickness of 15.322(6) Å and are parallel to the crystallographic *ab* plane, displaying channels along the *a* direction. The asymmetric unit (Figure S9) in this structure contains half a metal atom (Yb is placed at an inversion center) and one organic ligand. This only ligand in the asymmetric unit ligand displays one half of the carboxylic hydrogen atom bonded to the oxygen atom O2, due to the random distribution of the monoprotonated $(HL^4)^{1-}$ and deprotonated $(L^4)^{2-}$ ligands. The metal is coordinated to six oxygen atoms (O1, O3, O4, O1′, O3′, O4′) from six different organic linkers in a MO_6 octahedral coordination environment (Figure S10 and Table S13). The octahedra are placed at 4.706 Å in rows along *a*, joined by carboxylic bridges, while the distance between polyhedra separated by the full length of the organic linker is 10.559 Å. Both $(L^4)^{2-}/(HL^4)^{1-}$ ligands are coordinated to three different metals from two different rows in a tridentate μ_3-1κO;2κO′;3κO″ fashion. The strongest hydrogen bonds (Table S14) are observed within the layers, as shown in Figure 2, between the protonated and deprotonated non-coordinated O2 atoms (Table S14). It is remarkable that the planarity of the organic ligand is largely retained, not only in the Pz-Py-Pz moiety (with Pz-Py angles 1.90° and 3.50°, and Pz-Pz of 4.48°) but also, in the mono-coordinated carboxylic group (O1-C9-O2), with a maximum deviation from the Pz-Py-Pz plane of 0.251 Å for the non-coordinated O2.

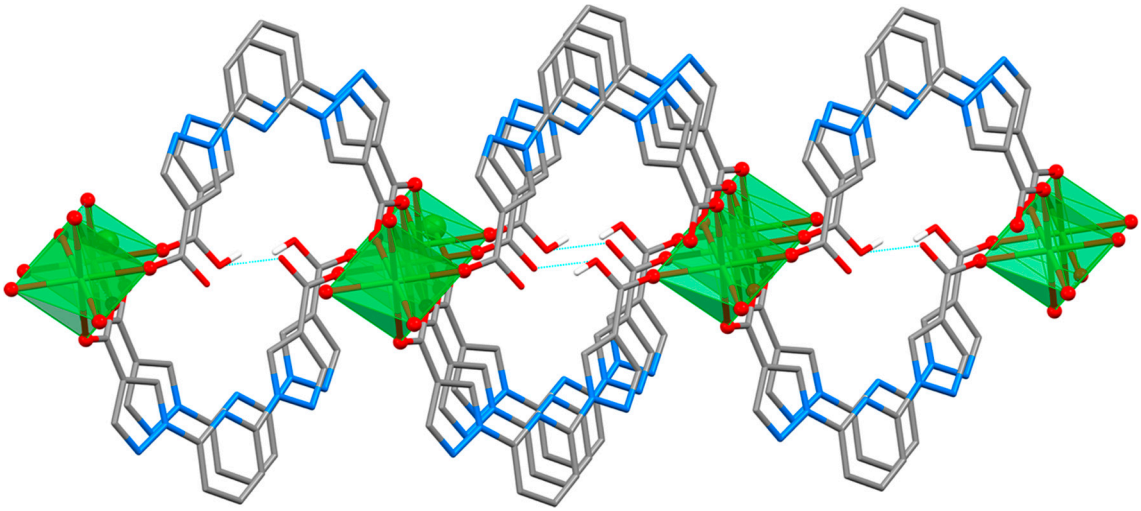

Figure 2. Lateral view of a layer of $[Yb(L^4)(HL^4)]_n$ in YbL^4, with hydrogen bonds shown as dotted lines in cyan.

Mixed lanthanide MOF Tb/YbL^3 (Figure 3) is a one-dimensional coordination polymer with formula $[M_2(L^3)_3(H_2O)_3]_n$ 2.5n(H_2O). The crystals contain double chains parallel to the *ac* direction with partially ordered water molecules located between them, as well as disordered solvent that could not be included in the model. The asymmetric unit is quite large and includes two metal centers, three organic ligands, three coordinated water molecules, and two and a half interstitial water molecules. The occupations of these two positions for the metal atoms in the asymmetric unit were refined both with the Yb/Tb ratio 51%:49%, according to the TXRF measurements performed on the crystalline solid. In this coordination polymer, the metal position M1 displays a MO_9 coordination environment, while the environment of M2 is MO_4N_3, with a M-N distance to the nitrogen atom from the pyridine ring much longer than the other ones (Figure S14 and Table S17). The coordination polyhedra are placed in M1-M2 pairs sharing one triangular face (O2, O5, O11). In this structure, three different distances between metals can be observed: the shortest one between the metal centers of face-sharing polyhedra (M1-M2 = 3.885 Å), while the longer M1-M1 (17.162 Å) and M2-M2 (17.098 Å) distances are observed between metals separated by the length of the $(L^3)^{2-}$ organic linkers. The $(L^3)^{2-}$ ligands show different coordination modes: two of them are linked to three different metals from two different pairs in a tridentate μ_3-1κ^2O,O′;2κO′′;2:3κO′′′ fashion, and the other one displays a μ_2-1κ^4O,N,N′,N′′;1:2κO′ mode. The packing of the coordination polymers in this crystal structure is the least dense of the four MOFs obtained; there are only weak hydrogen bonds between the chains and the interstitial water molecules. Also π–π interactions are observed between the $(L^3)^{2-}$ ligands next to each other along the chains. Regarding the planarity of the organic moiety, the pyrazole-pyridine angles vary from 3.03° to 12.26° and the pyrazole-pyrazole values from 4.44° to 15.92°.

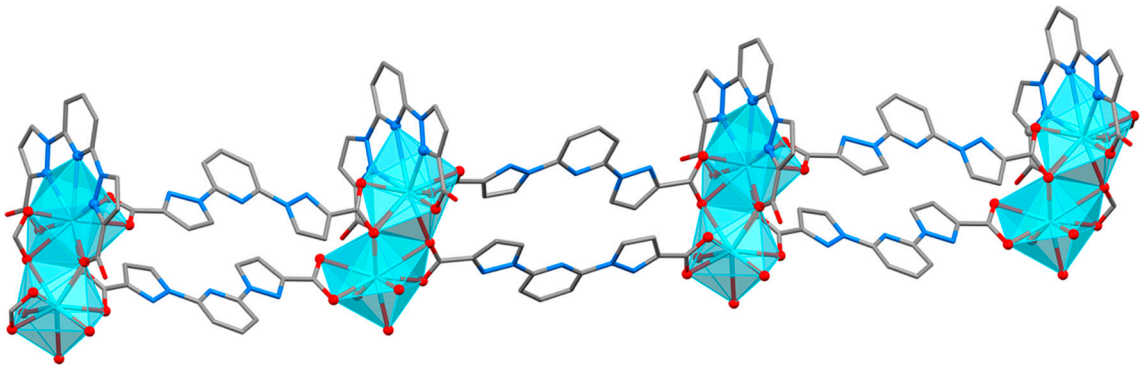

Figure 3. Chain of $[M_2L_3(H_2O)_3]_n$ in Tb/YbL^3.

Compound Tb/YbL^4 (Figure 4) is also a one-dimensional coordination polymer, with formula $[M(HL^4)(NO_3)_2]_n$, formed by chains parallel to the *ac* direction. The asymmetric unit (Figure S18) contains one half a metal center, one half of the organic ligand (both coincident with a two-fold rotation axis) and one chelating nitrate. The carboxylic hydrogen atom bonded to oxygen atom O2 shows a 50% occupation, as there is a random orientation of the protonated acid groups of the $(HL^4)^{1-}$ ligands. The position for the metal atoms was refined with partial occupations of Yb/Tb 62%:38%, according to the TXRF results performed on the crystalline solid. The metal position displays a MO_6N_3 coordination environment with the three nitrogen atoms (N1, N3, N3′) from one $(HL^4)^{1-}$ ligand, two oxygen atoms (O1, O1′) from two different organic linkers, and four oxygen atoms (O3, O4, O3′, O4′) from two nitrate ions. It is important to note that in this structure all of the metal atoms are located at the same distance (7.786 Å) from the nearest two neighbors. Although this distance is not the shortest one found in the four MOFs, it is remarkable that the bridge between the metal centers is comprised of a part of the ligand capable of delocalizing the electron density between adjacent lanthanides to give rise to an unbroken chain of communicating polyhedra along the full length of the coordination polymer. The $(HL^4)^{1-}$ ligand in this MOF shows a coordination mode μ_3-1κO;2κ^{3}N,N′,N″;3κO′. There are hydrogen bonds within the coordination polymer similar to the ones between non-coordinated O2 atoms in YbL^4, and there are also hydrogen interactions between MOFs, yielding a compact packing (Table S22). The organic ligand deviates largely from the planarity, with the largest angle values: the Pz-Py angle is 17.39°, and the Pz-Pz one is 30.18°.

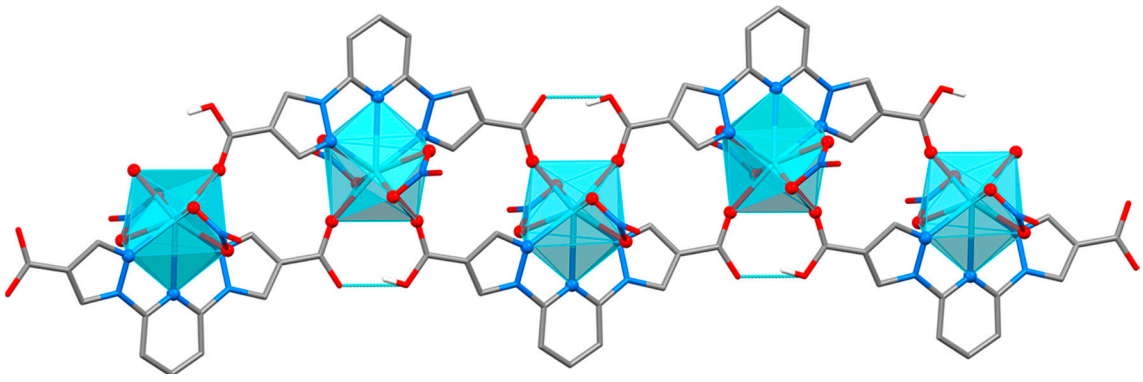

Figure 4. Chain of $[M(HL^4)(NO_3)_2]_n$ in Tb/YbL^4, with hydrogen bonds shown as dotted lines in cyan.

A topological analysis of the four MOFs was performed with TOPOS software [21] to compare the different arrangements, considering both the metal centers and organic ligands as nodes (Figure 5). The resulting underlying nets for the ytterbium derivatives were a uninodal 2D triconnected hcb net with symbol $\{6^3\}$ for YbL^3 and a 2D binodal tri, hexa-connected kgd net with symbol $\{4^3\}_2\{4^6.6^6.8^3\}$ for YbL^4. For the mixed metal MOFs, both underlying 1D nets are new topologies: in the case of

Tb/YbL^3 it is a (2,3,4)-connected trinodal one with symbol $\{4^2.6\}_2\{4^4.6^2\}_2\{4\}$, while Tb/YbL^4 displays a triconnected uninodal $\{4^2.6\}$ topology.

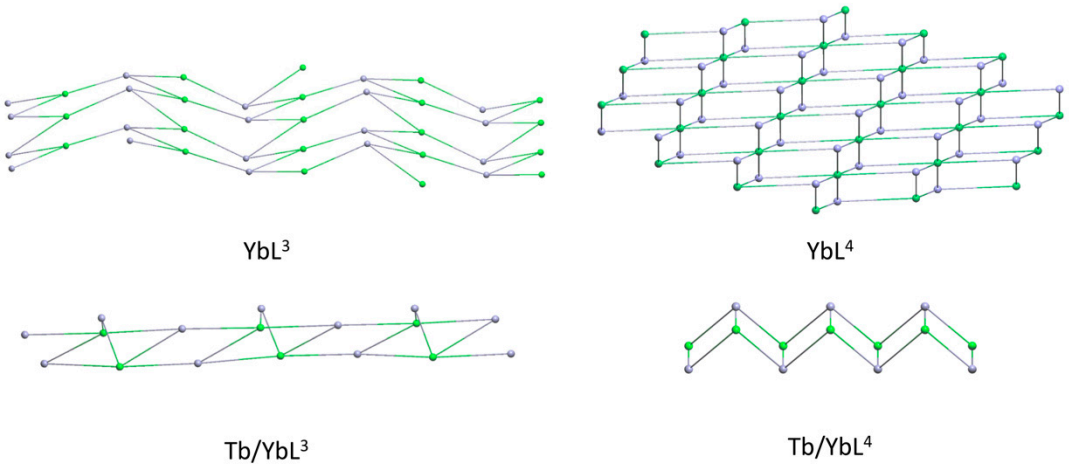

Figure 5. Underlying nets found in the MOFs considering as nodes the metal centers (green spheres) and the ligands (grey spheres).

Regarding the non-covalent interactions, it is significant that in the two MOFs derived from the L^4 ligand, O-H···O bonds are established between the protonated and deprotonated oxygen atoms that do not coordinate to the metal centers. These interactions strengthen the coordination framework and reinforce the resulting MOFs, as proved by the higher stability of these compounds compared to the L^3 derivatives. This is also the cause of the partial deprotonation of the H_2L^4 molecule to yield $(HL^4)^{1-}$ under the reaction conditions used for the obtention of the MOFs, while the H_2L^3 diacid loses both carboxylic hydrogen atoms.

It is also interesting to note that the disposition for 2,6-bis(pyrazol-1-yl)pyridine fragment adopted in the four new MOFs by most of the ligands is different to the one exhibited by related organic ligands found in the literature [22]. In the compounds reported by Halcrow et al., the coordination of the ligand is always of the chelating κ^3N,N′,N″ type, with the three nitrogen atoms facing towards the inside of the cavity. However, in YbL^3 and YbL^4, these three nitrogen atoms are located facing to opposite sides, and only in the mixed metal MOFs Tb/YbL^3 and Tb/YbL^4 κ^3N,N′,N″coordination mode is observed. This is mainly due to the addition of the carboxylate groups to the Pz-Py-Pz core, and the affinity of lanthanide metals for oxygen atoms.

3.2. Luminescence Properties

The four MOFs obtained present very different luminescent behavior, as expected from their also varied crystal structures. As anticipated from their coordination environment, the pure Yb(III) MOFs with L^3 and L^4 did not present significative NIR emission when the crystals were excited at the absorption wavelength of the chromophore (around 330 nm). As it has been discussed, in none of these two structures the heterocyclic rings participate in the coordination of Yb(III), and only the carboxylic oxygen atoms coordinate to the metals. In case of YbL^3, the octacoordinated Yb(III) ion completes its coordination sphere with two water molecules and one nitrate ion, whereas in YbL^4, the metal displays also an octahedral environment with six oxygen atoms from different organic ligands.

Combination of Tb(III) and Yb(III) in the crystalline MOFs yields a totally different panorama: as it has been described above, the mixed Tb/Yb MOFs with L^3 and L^4 present different structures where the most important modification of Tb/Yb MOFs compared to the pure Yb(III) MOFs is that, in both cases, coordination through the nitrogen atoms from the heterocycles is observed. In the case of Tb/YbL^3, two different coordination environment exist, one metal atom octacoordinated through five oxygen atoms from carboxylate groups and three water molecules, while the second one is nonacoordinated,

with seven oxygen atoms from carboxylate groups, plus two nitrogen atoms from pyrazole rings, and no water molecules are present in the coordination sphere of this second metal center. For Tb/YbL^4 only a unique nonacoordinated environment is observed with cooperative participation of the three nitrogen atoms from the pyridine and pyrazole rings, two nitrate ions and two oxygen atoms from carboxylate groups coming from two different linkers, and again without water molecules around the lanthanides. Clearly in Tb/YbL^4, lanthanide ions are expected to be statistically distributed as only one coordination environment is observed, whereas for Tb/YbL^3 a preference of Tb(III) or Yb(III) for each different coordination environment could not be discarded, as it was not possible to assign the preferential occupations of these ions in both coordination sites.

For Tb/YbL^3, only Tb(III) emission is observed when crystals are excited at the absorption maximum of the chromophore (330 nm) and no signal is detected for the Yb(III) ion. Ytterbium, unlike its Tb(III) counterpart, is more sensitive to vibronic deactivation from coordinating water molecules. Consequently, although Tb(III) is sensitized by the ligand, the energy transferred from it is only observed as emission of this ion, and in case the energy is transferred to Yb(III), it would be quenched by the OH vibronic couplings. A very different behavior occurs for Tb/YbL^4: Yb(III) NIR emission is observed when the sample is excited at the wavelength of the absorption maximum of the chromophore (338 nm). At this wavelength it is also possible to observe the typical emission pattern of Tb(III), with peaks assigned to the $^5D_4 \rightarrow {}^7F_J$ (J = 6,5,4,3) in addition to the NIR emission of Yb(III), as depicted in Figure 6.

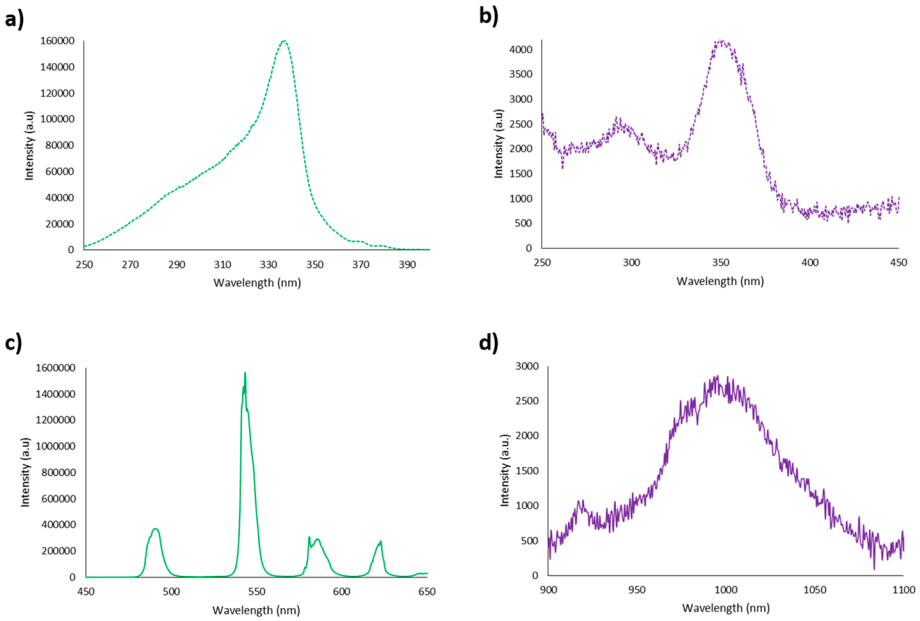

Figure 6. Luminescent behavior of Tb/Yb L^4. Excitation spectra at (**a**) λ_{em} = 545 nm (**b**) λ_{em} = 980 nm. Emission spectra at λ_{exc} = 338 nm (**c**) Tb(III) (**d**) Yb(III).

Figure 7 shows a simplified scheme of the energetic process that can be involved in the Tb/YbL^4 sample concerning the emission of Tb(III) and/or Yb(III). Starting from the excitation of the antenna chromophore bispyrazolepyridine (A), the system evolves by ISC (Inter System Crossing) to populate its triplet energy level (B) and from it, an energy transfer occurs towards the $^5D_4$ level of Tb(III) (C). The Tb(III) ion deexcites by the typical $^5D_4 \rightarrow {}^7F_J$ (J = 6,5,4,3) observed. From the excited $^5D_4$ Tb(III) level other processes could be taken into account when Yb(III) is present: one is the energy transfer towards $^2F_{5/2}$ level of Yb(III) (D), which is known as phonon-assisted energy transfer, whereas Tb(III) could also transfer its energy by means of a down conversion (DC) process [23,24] in which, from the transition $^5D_4 \rightarrow {}^7F_6$, corresponding to the emission observed at 493 nm, could be excited two Yb(III) ions (E). In addition, another process contrary to DC is the up-conversion (UC) [25–27] in which by

excitation of the $^2F_{7/2} \rightarrow {}^2F_{5/2}$ transition, two photons could excite the Tb(III) to its $^5D_4$ (F), with the corresponding higher energy emission.

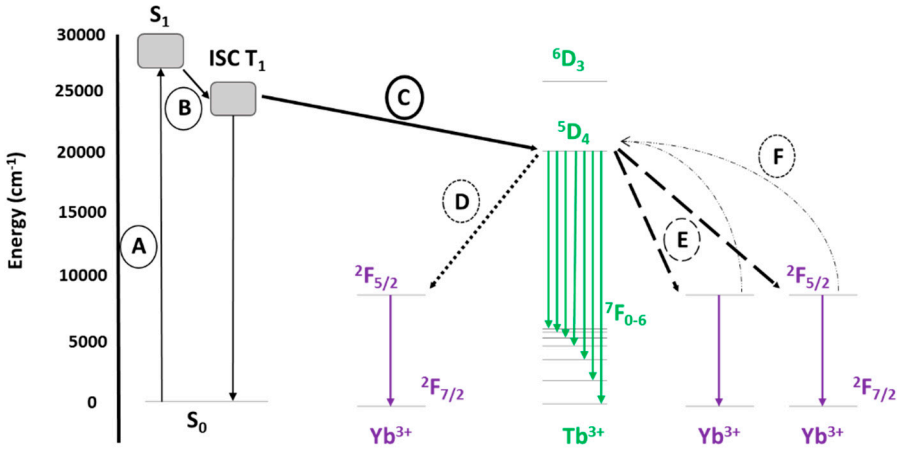

Figure 7. Proposed energy level diagram involving ligand Tb(III) and Yb(III) in the Tb/YbL^4 sample.

In the described chromophore/Tb/Yb system, several parallel energy migration processes could occur. As a consequence, they could result in two modal UV/Vis green or NIR excited luminescence. In our case, the emission observed indicates that some of these processes that involve the Yb(III) should be favored as consequence of the absence of water molecules coordinating Yb(III). UC green emission was not observed when crystals were excited at 980 nm and, in consequence, only sensitization of Yb(III) is observed when chromophore (338 nm) or Tb(III) (494 nm) are excited. Lifetimes measured at room temperature for the emission of Tb(III) and Yb(III) ions by excitation at these wavelengths are presented in Table 4.

Table 4. Lifetimes of the different Tb(III) and Yb(III) emissions observed.

Lifetimes	τ (μs)	Rel %
	Tb(III) λ_{exc} = 338 nm, λ_{ems} = 545 nm	
τ_1	610.1	31.6
τ_2	1485.7	64.4
	Yb(III) λ_{exc} = 494 nm, λ_{ems} = 980 nm	
τ_1	23.9	100
	Yb(III) λ_{exc} = 338 nm, λ_{ems} = 980 nm	
τ_1	99.4	100

The values for Tb(III) emission denote multiexponential decay curves indicating that several processes coexist simultaneously. These results need a more detailed study necessary to clarify the main mechanisms of the Yb(III) sensitization. Preparation of new MOFs with different Tb/Yb ratios and variable temperature spectroscopic studies with these samples are underway, in order to gain a deeper understanding of these new systems.

4. Conclusions

Four new lanthanide MOFs have been synthesized and characterized by several techniques and luminescence methods. The crystal structure of the organic ligands and the four resulting LnMOFs have been solved by SCXRD, observing that they present very different coordination characteristics as a consequence of both the geometrical disposition of the coordinating carboxylic acids in the ligands and the different metal ions present. Absence of water molecules in the coordination sphere of the hetero-lanthanide MOF Tb/YbL^4 originates an interesting material capable to sensitize

the intensely sought Yb(III) emission. Mechanisms behind this interesting emission needs to be adequately investigated.

Supplementary Materials: The following are available online at http://www.mdpi.com/2073-4352/10/2/69/s1. Figure S1: Molecule of H_2L^3 with atoms labelled in the asymmetric unit; Figure S2: Chain of molecules bonded by supramolecular interactions in the crystal of H_2L^3; Figure S3: Asymmetric unit with atoms labelled in the acetonitrile cocrystal of H_2L^4; Figure S4: Layer of molecules in H_2L^4; Figure S5: Asymmetric unit of YbL^3 with atoms labelled; Figure S6: Coordination environment of Yb(III) in YbL^3; Figure S7: IR spectrum of YbL^3; Figure S8: Blue: experimental diffractogram of YbL^3. Black: simulated powder diffractogram from SCXRD data with a random crystallite orientation; Figure S9: Asymmetric unit of YbL^4 with atoms labelled. Hydrogen atom in pink presents an occupation of 50% due to the random distribution in the crystal of $(HL^4)^{1-}$ and $(L4)^{2-}$ ligands; Figure S10: Coordination environment of Yb(III) in YbL^4; Figure S11: IR spectrum of YbL^4; Figure S12: Blue: experimental diffractogram of YbL^4. Grey: simulated powder diffractogram taking into account a (013) preferred orientation and a needle-like crystalline shape. Black: simulated powder diffractogram with a random crystallite orientation; Figure S13: Asymmetric unit of Tb/YbL^3 with atoms labelled; Figure S14: Coordination environments for M1 and M2 found in Tb/YbL^3; Figure S15: IR spectrum of Tb/YbL^3; Figure S16: Blue: experimental diffractogram of Tb/YbL^3. Black: simulated powder diffractogram with a random crystallite orientation. The green dot points out the most intense peak for the small impurity; Figure S17: Asymmetric unit of Tb/YbL^4 with atoms labelled. Hydrogen atom on pink presents an occupation of 50% due to the random distribution of the hydrogen atom in the MOF between the two carboxylic groups in each $(HL^4)^{1-}$ ligand; Figure S18: Coordination environment of the metal position Tb/YbL^4; Figure S19: IR spectra of Tb/YbL^4; Figure S20: Blue: experimental diffractogram of the solid obtained in the reaction of Tb and Yb with H_2L^4. Red: simulated powder diffractogram of the single crystal structure solved for Tb/YbL^4 with a random crystallite orientation. Light grey: simulated powder diffractogram of YbL^4 taking into account a (11-2) preferred orientation, and a needle-like crystalline shape. Black: simulated powder diffractogram of YbL^4 with a random crystallite orientation. The green dot points out the most intense peak for the small impurity. Table S1: Sample and crystal data for H_2L^3; Table S2: Data collection and structure refinement for H_2L^3; Table S3: Hydrogen bond parameters in H_2L^3 (Å, °); Table S4: Sample and crystal data for H_2L^4; Table S5: Data collection and structure refinement for H_2L^4; Table S6: Hydrogen bond parameters in H_2L^4 (Å, °), with the strongest interactions in bold italics; Table S7: Sample and crystal data for YbL^3 Table; S8: Data collection and structure refinement for YbL^3; Table S9: Coordination environment parameters in YbL^3; Table S10: Hydrogen bond parameters in YbL^3 (Å, °), with the strongest interactions in bold italics; Table S11: Sample and crystal data for YbL^4; Table S12: Data collection and structure refinement for YbL^4; Table S13: Coordination environment parameters in YbL^4; Table S14: Hydrogen bond parameters in YbL^4 (Å, °), with the strongest interactions in bold italics; Table S15: Sample and crystal data for Tb/YbL^3; Table S16: Data collection and structure refinement for Tb/YbL^3; Table S17: Coordination environment parameters in Tb/YbL^3; Table S18: Hydrogen bond parameters in Tb/YbL^3 (Å, °); Table S19: Sample and crystal data for Tb/YbL^4; Table S20: Data collection and structure refinement for Tb/YbL^4; Table S21: Coordination environment parameters in Tb/YbL^4; Table S22: Hydrogen bond parameters in Tb/YbL^4 (Å, °), with the strongest interaction in bold italics.

Author Contributions: Conceptualization, J.C.R.-U.; Methodology and experimental laboratory work, P.M.-M.; Writing—original draft preparation, review, and editing J.C.R.-U., P.M.-M., and J.P.; Structure solution, molecular graphics, and structural analysis, J.P.; Supervision, J.C.R.-U.; Project administration and funding acquisition, J.C.R.-U. All authors have read and agree to the published version of the manuscript.

Funding: The research leading to these results has received funding from ERCROS S.A. (Aranjuez, Spain).

Acknowledgments: Paloma Martinez-Martin thanks the scholarship received from UAM-ERCROS Chair for Pharmaceutical Chemistry. We wish to thank Prof. Loïc Charbonnière (Institut Pluridisciplinaire Hubert Curien, Strasbourg) for welcoming Paloma and helping to carry out the Yb(III) photophysical measurements, and Dr. Mario Ramírez (Single Crystal X-ray Diffraction Laboratory, SIdI-UAM) for his help in the analysis of the PXRD measurements.

Conflicts of Interest: The authors declare no conflict of interest.

References

1. Bunzli, J.-C.G.; Eliseeva, S.V. Intriguing aspects of lanthanide luminescence. *Chem. Sci.* **2013**, *4*, 1939–1949. [CrossRef]
2. Eliseeva, S.V.; Bunzli, J.-C.G. Lanthanide luminescence for functional materials and bio-sciences. *Chem. Soc. Rev.* **2010**, *39*, 189–227. [CrossRef]

3. Brites, C.D.S.; Lima, P.P.; Silva, N.J.O.; Millan, A.; Amaral, V.S.; Palacio, F.; Carlos, L.D. Thermometry at the nanoscale. *Nanoscale* **2012**, *4*, 4799–4829. [CrossRef]
4. Lanthanide Metal–Organic Frameworks. *Structure and Bonding 163*; Cheng, P., Ed.; Springer: Berlin/Heidelberg, Germany, 1985.
5. Yan, B. Lanthanide-Functionalized Metal-Organic Framework Hybrid Systems to Create Multiple Luminescent Centers for Chemical Sensing. *Acc. Chem. Res.* **2017**, *50*, 2789–2798. [CrossRef]
6. Rocha, J.; Carlos, L.D.; Almeida Paz, F.A.; Ananias, D. Luminescent Multifunctional Lanthanides-based Metalo-organic Frameworks. *Chem. Soc. Rev.* **2016**, *40*, 926–940. [CrossRef]
7. Weissman, S.I. Intramolecular energy transfer the fluorescence of complexes of europium. *J. Chem. Phys.* **1942**, *10*, 214–217. [CrossRef]
8. Chen, D.-H.; Haldar, R.; Neumeier, B.L.; Fu, Z.-H.; Feldmann, C.; Woll, C.; Redel, E. Tunable Emission in Heteroepitaxial Ln-SURMOFs. *Adv. Funct. Mater.* **2019**, *29*, 1903086. [CrossRef]
9. De Lill, D.T.; Bettencourt-Dias, A.; Cahill, C.L. Exploring Lanthanide Luminescence in Metal–organic Frameworks: Synthesis, Structure, and Guest-Sensitized Luminescence of a Mixed Europium/Terbium-Adipate Framework and a Terbium-Adipate Framework. *Inorg. Chem.* **2007**, *46*, 3960–3965. [CrossRef]
10. Martinez, P.; Perles, J.; Rodriguez Ubis, J.C. Under preparation.
11. Grzyb, T.; Gruszeczka, A.; Wiglusz, R.J.; Sniadecki, Z.; Idzikowski, B.; Lisa, S. Multifunctionality of $GdPO_4$:Yb^{3+}, Tb^{3+}nanocrystals – luminescence and magnetic behavior. *J. Mater. Chem.* **2012**, *22*, 22989–22997. [CrossRef]
12. Debasu, M.L.; Ananias, D.; Rocha, J.; Malta, O.L.; Carlos, L.D. Energy-transfer from Gd(iii) to Tb(iii) in (Gd,Yb,Tb)PO_4 nanocrystals. *Phys. Chem. Chem. Phys.* **2013**, *15*, 15565–15571. [CrossRef]
13. Enrichi, F.; Armellini, C.; Belmokhtar, S.; Bouajaj, A.; Chiappini, A.; Ferrari, M.; Quandt, A.; Righini, G.C.; Vomiero, A.; Zur, L. Visible to NIR downconversion process in Tb^{3+}-Yb^{3+} codoped silica-hafnia glass and glass-ceramic sol–gel waveguides for solar cells. *J. Lumin.* **2018**, *193*, 44–50. [CrossRef]
14. Terra, I.A.A.; Borrero-Gonzalez, L.J.; Figueredo, T.R.; Almeida, J.M.P.; Hernandes, A.C.; Nunes, L.A.O.; Malta, O.L. Down-conversion process in Tb3+ –Yb3+ co-doped Calibo glasses. *J. Lumin.* **2012**, *132*, 1678. [CrossRef]
15. Martin, I.R.; Yanes, A.C.; Mendez-Ramos, J.; Torres, M.E.; Rodriguez, V.D. Cooperative energy transfer in Yb^{3+}–Tb^{3+} codoped silica sol–gel glasses. *J. App. Phys.* **2001**, *89*, 2520. [CrossRef]
16. Andres, P.R.; Schubert, U.S. New Functional Polymers and Materials Based on 2,2′:6′,2″-Terpyridine Metal Complexes. *Adv. Mater.* **2004**, *16*, 1043–1068. [CrossRef]
17. Halcrow, M.A. Recent advances in the synthesis and applications of 2,6-dipyrazolylpyridine derivatives and their complexes. *New J. Chem.* **2014**, *38*, 1868–1882. [CrossRef]
18. Basak, S.; Chandrasekar, R. Multiluminescent Hybrid Organic/Inorganic Nanotubular Structures: One-Pot Fabrication of Tricolor (Blue–Red–Purple) Luminescent Parallepipedic Organic Superstructure Grafted with Europium Complexes. *Adv. Funct. Mater.* **2011**, *21*, 667–673. [CrossRef]
19. Remuiñan, M.; Román, H.; Alonso, M.T.; Rodriguez-Ubis, J.C. Synthesis and Luminiscence Properties of Europium(m) and Terbium(m) Complexes with Polyacid Chelates Derived from 2,6-Bis(N-pyrazolyl)pyridine. *J. Chem. Soc. Perkin Trans. 2* **1993**, 1099–1102. [CrossRef]
20. Dollase, W.A. Correction of intensities for preferred orientation in powder diffractometry: Application of the March model. *J. Appl. Cryst.* **1986**, *19*, 267–272. [CrossRef]
21. Blatov, V.A.; Shevchenko, A.P.; Proserpio, D.M. Applied topological analysis of crystal structures with the program package ToposPro. *Cryst. Growth Des.* **2014**, *14*, 3576–3586. [CrossRef]
22. Elhaïk, J.; Evans, D.J.; Kilnera, C.A.; Halcrow, M.A. A structural, magnetic and Mössbauer spectroscopic study of an unusual angular Jahn–Teller distortion in a series of high-spin iron(II) complexes. *Dalton Trans.* **2005**, 1693–1700. [CrossRef]
23. Wang, H.; Ye, S.; Lui, T.; Li, S.; Hu, R.; Wang, D. Influence of local phonon energy on quantum efficiency of Tb^{3+}-Yb^{3+} co-doped glass ceramics containing fluoride nanocrystals. *J. Rare Earths* **2015**, *33*, 524–528. [CrossRef]
24. Belmokhtar, S.; Bouajaj, A.; Britel, M.; Normani, S.; Armellini, C.; Boulard, B.; Enrichi, F.; Belluomo, F.; Di Stefano, A.; Ferrari, M. Energy transfer from Tb^{3+} to Yb^{3+} in silica hafinia glass ceramic for photovoltaic applications. *J. Mater. Environ. Sci.* **2016**, *7*, 515–518.

25. Dong, H.; Sun, L.-D.; Wang, Y.-F.; Xiao, J.-W.; Tu, D.; Chen, X.; Yan, C.-H. Photon upconversion in Yb^{3+}–Tb^{3+} and Yb^{3+}–Eu^{3+} activated core/shell nanoparticles with dual-band excitation. *J. Mater. Chem. C.* **2016**, *4*, 4186–4192. [CrossRef]
26. Grzyb, T. Bright and tunable up-conversion luminescence through cooperative energy transfer in Yb^{3+}, Tb^{3+} and Eu^{3+} co-doped $LaPO_4$ nanocrystals. *RSC Adv.* **2014**, *4*, 2590–2595. [CrossRef]
27. Tao, L.; Zhao, Y.; Li, J. Photon upconversion in Yb/Tb co-sensitized core-shell nanocrystals by interfacial energy transfer. *Opt. Mater. Express* **2017**, *7*, 1022–1028. [CrossRef]